Appl. Math. Mech. -Engl. Ed., **36**(9), 1169–1184 (2015)
DOI 10.1007/s10483-015-1973-6

Applied Mathematics and Mechanics (English Edition)

Buoyant Marangoni convection of nanofluids in square cavity*

H. SALEH[1,†], I. HASHIM[1,2,3]

1. School of Mathematical Sciences, Universiti Kebangsaan Malaysia,
43600 UKM Bangi Selangor, Malaysia;
2. Solar Energy Research Institute, Universiti Kebangsaan Malaysia,
43600 UKM Bangi Selangor, Malaysia;
3. Research Institute, Center for Modeling & Computer Simulation (RI/CM&CS),
King Fahd University of Petroleum & Minerals, Dhahran-31261, Saudi Arabia

Abstract The buoyant Marangoni convection heat transfer in a differentially heated cavity is numerically studied. The cavity is filled with water-Ag, water-Cu, water-Al_2O_3, and water-TiO_2 nanofluids. The governing equations are based on the equations involving the stream function, vorticity, and temperature. The dimensionless forms of the governing equations are solved by the finite difference (FD) scheme consisting of the alternating direction implicit (ADI) method and the tri-diagonal matrix algorithm (TDMA). It is found that the increase in the nanoparticle concentration leads to the decrease in the flow rates in the secondary cells when the convective thermocapillary and the buoyancy force have similar strength. A critical Marangoni number exists, below which increasing the Marangoni number decreases the average Nusselt number, and above which increasing the Marangoni number increases the average Nusselt number. The nanoparticles play a crucial role in the critical Marangoni number.

Key words finite difference method, Marangoni convection, nanofluid

Chinese Library Classification O353.4
2010 Mathematics Subject Classification 76D45

1 Introduction

In 1900, Henri Bénard, a French physicist, demonstrated that the attractive hexagonal structure could be obtained by a simple experiment[1]. Later, Pearson[2] identified that the Bénard cells were driven by the imbalance of the tangential stress on the interface caused by the temperature dependence of the surface tension. He also concluded that the character of the response of the fluid depended on the overall heat transport in the flow system, and the fluid motion could be induced through an instability process. The fluid motion along a free surface due to the surface tension effect is a common phenomenon in many material processes such as crystal growth, droplet vaporizing, and electron beam melting. Such flow is known either as thermocapillary flow or Marangoni convection. Marangoni convection is dominant for

---

* Received Jul. 8, 2014 / Revised Jan. 9, 2015
Project supported by the Fundamental Research Grant Scheme of the Ministry of Education of Malaysia (No. FRGS/1/2014/SG04/UKM/01/1) and the Dana Impak Perdana of Universiti Kebangsaan Malaysia (No. DIP-2014-015)

† Corresponding author, E-mail: Dr.habibissaleh@gmail.com

a small-scale system or in low-gravity hydrodynamics. The surface tension driven flows also occur in the respiratory system, where the air penetrates into the lung, resulting in the open of the airways, which thus makes the interior superior of the airways be coated with a thin lining fluid.

Strani et al.[3] studied the buoyant Marangoni convection in a cavity, and concluded that the surface deformation had a negligible effect on the qualitative aspects of the flow-field structure at a low crispation number. Srinivasan and Basu[4] found that the buoyancy driven flow was negligible compared with the surface tension gradient driven flow in laser melting. Bergman and Ramadhyani[5] numerically investigated the characteristics of the buoyancy driven flow in a square cavity, and showed that the surface tension significantly altered the buoyant flow. Carpenter and Homsy[6] established the boundary layer scalings for the buoyant and thermocapillary convection. Hadid and Roux[7] analyzed a shallow cavity, and showed that the surface tension had a quite significant effect on the stability of a primary buoyancy driven flow. Rudraiah et al.[8] and Hossain et al.[9] studied the effects of a magnetic field on the combined convection. Saleem et al.[10] examined a square cavity, whose right wall was kept open for the flow entrainment and exit.

Most of the studies on the buoyant Marangoni convection in cavities have considered the pure fluid. In recent years, a new type of nanoparticles has been introduced, and followed by engineered nanofluids[11]. Nanofluids such as water-Cu, water-CuO, water-Cu, water-Al_2O_3, water-TiO_2, and water-Ag have been utilitized by Khanafer et al.[12], Jou and Tzeng[13], Das and Ohal[14], Ghasemi and Aminossadati[15], Oztop and Abu-Nada[16], and Öğüt[17] to increase the heat transfer performance of the natural convection without thermocapillary effects. Hwang et al.[18], Santra et a.[19], and Rashmi et al.[20] studied the convection with nanoparticles for a particular Rayleigh number. Ho et al.[21] investigated the effects of the uncertainties due to the adoption of different formulas for the ratio of thermal conductivity and dynamic viscosity for water-Al_2O_3 nanofluids, and found that the heat transfer could be enhanced or mitigated because of the use of nanofluids. Qi et al.[22] and He et al.[23] found that the flow and heat transfer characteristics of nanofluids were more sensitive to viscosity than to thermal conductivity. Fattahi et al.[24] used a new model for the conductivity of water-Cu nanofluids in a differentially heated square enclosure, where the thermocapillary was neglected. In the present study, the buoyant thermocapillary convection of the nanofluids with different nanoparticles is considered.

2 Mathematical formulation

Consider a square cavity shown in Fig. 1. The left wall is kept at a low temperature ($T_{\rm c}$), the right wall is kept at a high temperature ($T_{\rm h}$), and the bottom and top walls are adiabatic. The top free surface is assumed to be flat and non-deformable.

The surface tension σ on the upper boundary is assumed to vary linearly with the temperature, and it can be expressed by

$$\sigma = \sigma_0(1 - \gamma(T - T_0)), \tag{1}$$

where T_0 is a reference temperature defined by

$$T_0 = \frac{1}{2}(T_{\rm h} + T_{\rm c}).$$

γ is the temperature coefficient of the surface tension defined by

$$\gamma = \frac{1}{\sigma_0}\frac{\partial \sigma}{\partial T},$$

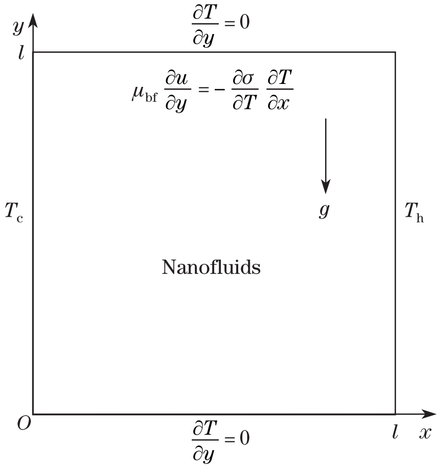

Fig. 1 Schematic representation of model

where σ_0 is a reference surface tension, and T is the temperature of the fluid in the cavity. The fluid in the enclosure is a water-based nanofluid containing Ag, Cu, and Al_2O_3 or TiO_2 nanoparticles. The fluid is assumed to be Newtonian and incompressible. The flow is unsteady and laminar. We assume that there is no internal heat generation, absorption, or viscous dissipation. No-slip velocity conditions are imposed on all the boundaries except the case where the top wall is slip or symmetric. The direction of the gravitational force is in the negative y-direction. Under the above assumptions, the conservation equations for the mass, momentum, and energy are

$$\frac{\partial u}{\partial x}+\frac{\partial v}{\partial y}=0, \tag{2}$$

$$\frac{\partial u}{\partial t}+u\frac{\partial u}{\partial x}+v\frac{\partial u}{\partial y} = -\frac{1}{\rho_{\rm nf}}\frac{\partial p}{\partial x}+\frac{\mu_{\rm nf}}{\rho_{\rm nf}}\Big(\frac{\partial^2 u}{\partial x^2}+\frac{\partial^2 u}{\partial y^2}\Big), \tag{3}$$

$$\frac{\partial v}{\partial t}+u\frac{\partial v}{\partial x}+v\frac{\partial v}{\partial y} = -\frac{1}{\rho_{\rm nf}}\frac{\partial p}{\partial y}+\frac{\mu_{\rm nf}}{\rho_{\rm nf}}\Big(\frac{\partial^2 v}{\partial x^2}+\frac{\partial^2 v}{\partial y^2}\Big)+g\beta_{\rm nf}(T-T_{\rm c}), \tag{4}$$

$$\frac{\partial T}{\partial t}+u\frac{\partial T}{\partial x}+v\frac{\partial T}{\partial y} = \alpha_{\rm nf}\Big(\frac{\partial^2 T}{\partial x^2}+\frac{\partial^2 T}{\partial y^2}\Big), \tag{5}$$

where u and v are the velocity components in the x- and y-directions, respectively. p is the pressure, α is the thermal diffusivity, and β is the thermal expansion coefficient. The subscript nf denotes nanofluids. The appropriate initial boundary conditions are

$$u = v = 0, \quad T = T_{\mathrm{c}} \quad \text{at} \quad t = 0 \quad \text{for the whole enclosure,} \tag{6}$$

$$u = v = 0, \quad T = T_{\mathrm{c}} \quad \text{at} \quad x = 0, \tag{7}$$

$$u = v = 0, \quad T = T_{\mathrm{h}} \quad \text{at} \quad x = \ell, \tag{8}$$

$$u = v = 0, \quad \frac{\partial T}{\partial y} = 0 \quad \text{at} \quad y = 0, \tag{9}$$

$$v = 0, \quad \frac{\partial T}{\partial y} = 0, \quad \mu_{\mathrm{bf}} \frac{\partial u}{\partial y} = -\frac{\partial \sigma}{\partial T}\frac{\partial T}{\partial x} \quad \text{at} \quad y = \ell. \tag{10}$$

The dynamic boundary conditions on the top free surface relate the velocity gradient to the temperature gradient. This represents the balance between the shear stress and the surface tension gradient at the surface which is responsible for the establishment of the thermocapillary flow in the cavity. The effect of the interface deformability is not considered here. The shape of the gas-liquid interface depends on the buoyancy force and the pressure force. For pure buoyancy flow, the pressure is higher in the upper hot corner, and consequently there is an elevation of the free boundary in this corner and a depression near the cold corner. For pure thermocapillary flow, the opposite effect will appear.

The effective density of the nanofluids ρ_{nf} is given as follows:

$$\rho_{\mathrm{nf}} = (1-\phi)\rho_{\mathrm{bf}} + \phi\rho_{\mathrm{sp}}, \tag{11}$$

where the subscripts bf and sp denote the basefluid and the solid particles, respectively. ϕ is the solid volume fraction of the nanoparticles. The thermal diffusivity of the nanofluids is

$$\alpha_{\mathrm{nf}} = \frac{k_{\mathrm{nf}}}{(\rho c_p)_{\mathrm{nf}}}, \tag{12}$$

where the heat capacitance of the nanofluids is

$$(\rho c_p)_{\mathrm{nf}} = (1-\phi)(\rho c_p)_{\mathrm{bf}} + \phi(\rho c_p)_{\mathrm{sp}}. \tag{13}$$

The thermal expansion coefficient of the nanofluids can be determined by

$$\beta_{\mathrm{nf}} = (1-\phi)\beta_{\mathrm{bf}} + \phi\beta_{\mathrm{sp}}. \tag{14}$$

The ratio dynamic viscosity of the nanofluids given by Brinkman[25] is

$$\frac{\mu_{\mathrm{nf}}}{\mu_{\mathrm{bf}}} = \frac{1}{(1-\phi)^{\frac{5}{2}}}. \tag{15}$$

The ratio thermal conductivity of the nanofluids restricted to the spherical nanoparticles is approximated by the Maxwell-Garnetss (MG)[17] model as follows:

$$\frac{k_{\mathrm{nf}}}{k_{\mathrm{bf}}} = \frac{k_{\mathrm{sp}} + 2k_{\mathrm{bf}} - 2\phi(k_{\mathrm{bf}} - k_{\mathrm{sp}})}{k_{\mathrm{sp}} + 2k_{\mathrm{bf}} + \phi(k_{\mathrm{bf}} - k_{\mathrm{sp}})}. \tag{16}$$

The viscosity and conductivity of the nanofluids are integrated in Fig. 2, and the physical properties of the water and nanoparticles are given in Table 1.

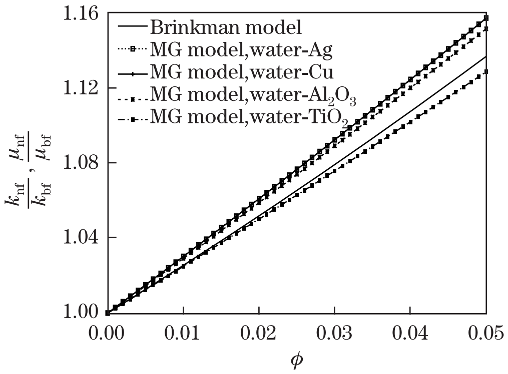

Fig. 2 Ratio thermal conductivity of water-Ag, water-Cu, water-Al$_2$O$_3$, and water-TiO$_2$ by use of MG model and ratio dynamical viscosity by use of Brinkman model versus volume fraction

Table 1 Thermo-physical properties of water with Cu[12], Al$_2$O$_3$[21], Ag, and TiO$_2$[17]

Physical property	Water	Ag	Cu[12]	Al$_2$O$_3$[21]	TiO$_2$[17]
$c_p/(\mathrm{J}\cdot(\mathrm{kg})^{-1}\cdot\mathrm{K}^{-1})$	4 179	235	383	765	686.2
$\rho/(\mathrm{kg}\cdot\mathrm{m}^{-3})$	997.1	10 500	8 954	3 600	4 250
$k/(\mathrm{W}\cdot\mathrm{m}^{-1}\cdot\mathrm{K}^{-1})$	0.6	429	400	46	8.954
$\beta\times10^{-5}/(\mathrm{K}^{-1})$	21	5.4	1.67	0.63	2.4

The governing equations given above are in terms of the so-called primitive variables, i.e., u, v, p, and T. The solution procedure discussed in this work is based on the equations involving the stream function ψ, the vorticity ω, and the temperature T. Some of them are defined by

$$u=\frac{\partial\psi}{\partial y},\quad v=-\frac{\partial\psi}{\partial x},\quad \omega=\frac{\partial v}{\partial x}-\frac{\partial u}{\partial y}.$$

We first eliminate the pressure between the two momentum equations, then write the obtained results in the stream function, vorticity, and temperature formulation, and finally perform nondimensionalization. Then, we can rewrite Eqs. (2)–(5) as follows:

$$\frac{\partial^2\Psi}{\partial X^2}+\frac{\partial^2\Psi}{\partial Y^2}=-\Omega, \tag{17}$$

$$\begin{aligned}&\frac{\partial\Omega}{\partial\tau}+\frac{\partial\Psi}{\partial Y}\frac{\partial\Omega}{\partial X}-\frac{\partial\Psi}{\partial X}\frac{\partial\Omega}{\partial Y}\\ =&\frac{Pr_{\mathrm{bf}}}{(1-\phi)^{\frac{5}{2}}(1-\phi+\phi\frac{\rho_{\mathrm{sp}}}{\rho_{\mathrm{bf}}})}\Big(\frac{\partial^2\Omega}{\partial X^2}+\frac{\partial^2\Omega}{\partial Y^2}\Big)\\ &+Ra_{\mathrm{bf}}Pr_{\mathrm{bf}}\Big(1-\phi+\phi\frac{\beta_{\mathrm{sp}}}{\beta_{\mathrm{bf}}}\Big)\frac{\partial\Theta}{\partial X},\end{aligned} \tag{18}$$

$$\begin{aligned}&\frac{\partial\Theta}{\partial\tau}+\frac{\partial\Psi}{\partial Y}\frac{\partial\Theta}{\partial X}-\frac{\partial\Psi}{\partial X}\frac{\partial\Theta}{\partial Y}\\ =&\frac{\frac{k_{\mathrm{nf}}}{k_{\mathrm{bf}}}}{1-\phi+\phi\frac{(\rho c_p)_{\mathrm{sp}}}{(\rho c_p)_{\mathrm{bf}}}}\Big(\frac{\partial^2\Theta}{\partial X^2}+\frac{\partial^2\Theta}{\partial Y^2}\Big).\end{aligned} \tag{19}$$

The dimensionless initial and boundary conditions are

$$\Psi = 0, \quad \Omega = 0, \quad \Theta = 0 \quad \text{at} \quad \tau = 0 \quad \text{for the whole enclosure,} \tag{20}$$

$$\Psi = 0, \quad \Omega = -\frac{\partial^2 \Psi}{\partial X^2}, \quad \Theta = 0 \quad \text{at} \quad X = 0, \tag{21}$$

$$\Psi = 0, \quad \Omega = -\frac{\partial^2 \Psi}{\partial X^2}, \quad \Theta = 1 \quad \text{at} \quad X = 1, \tag{22}$$

$$\Psi = 0, \quad \Omega = -\frac{\partial^2 \Psi}{\partial Y^2}, \quad \frac{\partial \Theta}{\partial Y} = 0 \quad \text{at} \quad Y = 0, \tag{23}$$

$$\Omega = -\frac{\partial^2 \Psi}{\partial Y^2} = -Ma_{\mathrm{bf}} \frac{\partial \Theta}{\partial X}, \quad \frac{\partial \Theta}{\partial Y} = 0 \quad \text{at} \quad Y = 1, \tag{24}$$

where

$$\begin{cases} X = \dfrac{x}{l}, \quad Y = \dfrac{y}{l}, \quad \Psi = \dfrac{\psi}{\alpha_{\mathrm{bf}}}, \quad \Theta = \dfrac{T - T_{\mathrm{c}}}{T_{\mathrm{h}} - T_{\mathrm{c}}}, \\ Ma_{\mathrm{bf}} = -\dfrac{\partial \sigma}{\partial T} \dfrac{(T_{\mathrm{h}} - T_{\mathrm{c}})\ell}{\mu_{\mathrm{bf}} \alpha_{\mathrm{bf}}}, \quad Pr_{\mathrm{bf}} = \dfrac{\nu_{\mathrm{bf}}}{\alpha_{\mathrm{bf}}}, \\ Ra_{\mathrm{bf}} = \dfrac{g \beta_{\mathrm{bf}} (T_{\mathrm{h}} - T_{\mathrm{c}}) l^3}{\nu_{\mathrm{bf}} \alpha_{\mathrm{bf}}}, \quad P = \dfrac{p l^2}{\rho_{\mathrm{nf}} \alpha_{\mathrm{bf}}^2}, \quad \Omega = \dfrac{\omega l^2}{\alpha_{\mathrm{bf}}}. \end{cases} \tag{25}$$

Once we know the temperature, we can measure the heat transfer performance. The total heat transfer rate across the cavity in terms of the average Nusselt number ($\overline{Nu}$) is defined by

$$\overline{Nu}_{\mathrm{c}} = \int_0^1 \left(\frac{k_{\mathrm{nf}}}{k_{\mathrm{bf}}} \frac{\partial \Theta}{\partial X} \right)_{X=0} \mathrm{d}Y \quad \text{at the cold wall,} \tag{26}$$

$$\overline{Nu}_{\mathrm{h}} = \int_0^1 \left(\frac{k_{\mathrm{nf}}}{k_{\mathrm{bf}}} \frac{\partial \Theta}{\partial X} \right)_{X=1} \mathrm{d}Y \quad \text{at the hot wall.} \tag{27}$$

3 Numerical method and validation

The finite difference (FD) scheme, consisting of the alternating direction implicit (ADI) method and the tri-diagonal matrix algorithm (TDMA), is used to solve Eqs. (17) and (19) subject to Eqs. (20)–(24). The effect of the grid resolution is examined in order to select the appropriate grid density as demonstrated in Table 2 for water-Cu at $\phi = 0.03$, $Ma_{\mathrm{bf}} = 10^3$, and $Ra_{\mathrm{bf}} = 10^3$. The results indicate that a 110 × 110 mesh can be used in the final computation. As a validation, our results for the average Nusselt number agree well with those obtained by Ref. [9] for the special case $\phi = 0$ as shown in Table 3.

Table 2 Grid sensitivity check for water-Cu at $\phi = 0.03$, $Ma_{\mathrm{bf}} = 10^3$, and $Ra_{\mathrm{bf}} = 10^3$

Grid size	20 × 20	30 × 30	40 × 40	50 × 50	60 × 60	70 × 70
$\overline{Nu}_{\mathrm{c}}$	1.168 6	1.162 6	1.160 2	1.158 9	1.158 1	1.157 7
$\overline{Nu}_{\mathrm{h}}$	1.176 7	1.182 5	1.184 9	1.186 1	1.186 8	1.187 3

Grid size	80 × 80	90 × 90	100 × 100	110 × 110	120 × 120
$\overline{Nu}_{\mathrm{c}}$	1.141 2	1.141 0	1.140 8	1.124 9	1.124 8
$\overline{Nu}_{\mathrm{h}}$	1.204 2	1.204 5	1.204 6	1.221 1	1.221 2

Table 3 Results of $\overline{Nu}$ for $Ra_{\mathrm{bf}} = 1.08 \times 10^3$, $Pr_{\mathrm{bf}} = 0.054$, and $\phi = 0.00$

Ma_{bf}	Present	Ref. [7]
0	1.149 2	1.114 44
100	1.168 1	1.116 25
1 000	1.450 7	1.440 93

4 Results and discussion

The present work visualizes a surface tension and some nanofluid effects on a differentially heated square cavity. The fluid flow, temperature distribution, and overall heat transfer characteristics are analyzed through the streamlines, isotherms, and average Nusselt number at the cold and hot walls. The analysis in the undergoing numerical investigation is performed in the following ranges of associated dimensionless groups:

$$\begin{cases} 0 \leqslant Ma_{\mathrm{bf}} \leqslant 1\,000, \\ 0.00 \leqslant \phi \leqslant 0.05, \\ 10^3 \leqslant Ra_{\mathrm{bf}} \leqslant 10^4. \end{cases}$$

The present work will also compare the utilization of different nanoparticles, i.e., Ag, Cu, Al_2O_3, and TiO_2, as specified in Table 1. The flow and temperature fields of the nanofluids and the base fluid are shown in Figs. 3 and 4 for the steady state and in Figs. 5 and 6 for the unsteady condition, respectively. The corresponding average Nusselt numbers are presented in Figs. 7–9.

Figure 3 displays the evolutions of the fluid flow and temperature distribution in a differentially heated square cavity for water-Cu nanofluids with the volume fraction 3% and the pure water at different Marangoni numbers and $Ra_{\mathrm{bf}} = 10^3$. From the figure, we can see that the temperature of the right wall is higher than that of the nanofluids or the base fluids inside the cavity. Therefore, the wall transmits heat to the fluid, and raises the temperature of the fluid particles adjoining the right wall. When the temperature rises, the fluid starts moving from the right (hot) wall to the left (cold) wall and falling along the cold wall, then rises again at the hot wall, and creates a counter and single clockwise rotating cells in the cavity as shown in the streamline patterns. From the figure, we can also observe that the circulations of the nanofluid cells are smaller than those of the water cells. The relative small stress at the top surface does not affect the flow and temperature characteristics in the cavity. When the shear stress increases at the free surface $Ma_{\mathrm{bf}} = 100$, the intensity of the main flow at the bottom portion due to the gravity force weakens significantly. A secondary flow develops at the top portion of the cavity, and rotates in a clockwise direction. The strength of the flow circulations of the nanofluids is slightly weaker than that of the base fluid. The main cells of the nanofluids are smaller than the water cells. The main cells of the water are more suppressed to the bottom than those of the nanofluids. The negative signs in the streamlines refer to clockwise flow, and represent the surface tension effect. The positive signs in the streamlines refer to anti-clockwise flow, and represent the natural convection effect. With a further increase in the Marangoni number, e.g., $Ma_{\mathrm{bf}} = 1\,000$, as shown in Fig. 3(c), the surface tension induced shear increases the free surface velocity significantly, and therefore, the main flow weakens substantially first, and then becomes invisible. The strength of the secondary flow circulations of the nanofluids is slightly stronger than that of the base fluid. The isotherms are more distorted at the stronger Marangoni convection with denser boundary layers near the upper-right corner of the cavity. Moreover, adding the nanoparticles alters the temperature distribution at the lower and upper regions.

$(\Psi_{\max})_{\rm bf} = 1.37, \ (\Psi_{\max})_{\rm nf} = 1.53$

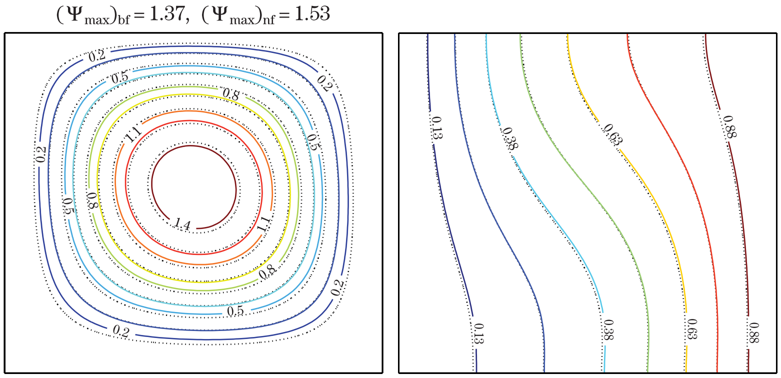

(a) Streamlines at $Ma = 10$ (b) Isotherms at $Ma = 10$

$(\Psi_{\min})_{\rm bf} = -0.355, \ (\Psi_{\min})_{\rm nf} = -0.302$

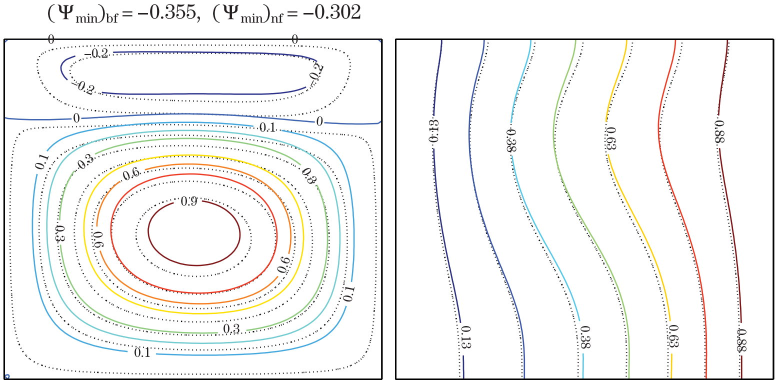

(c) Streamlines at $Ma = 100$ (d) Isotherms at $Ma = 100$

$(\Psi_{\min})_{\rm bf} = -4.35, \ (\Psi_{\min})_{\rm nf} = -4.49$

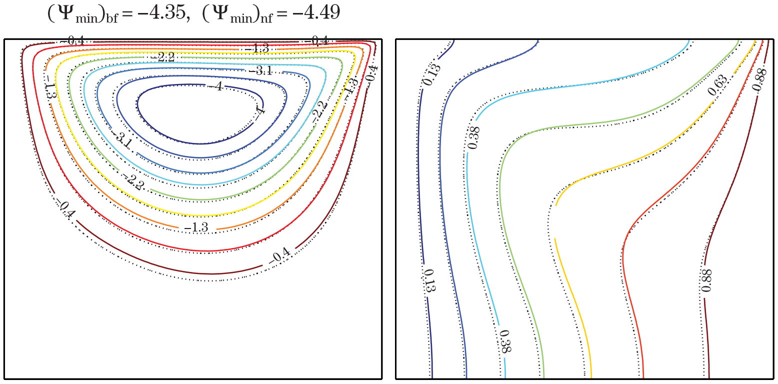

(e) Streamlines at $Ma = 1\,000$ (f) Isotherms at $Ma = 1\,000$

Fig. 3 Steady state streamlines and isotherms: water-Cu nanofluids with $\phi = 0.03$, solid lines; pure water for different Marangoni numbers at $Ra_{\rm bf} = 10^3$, dashed lines

Figure 4 displays the fluid flow and thermal characteristics inside the cavity for water-Cu nanofluids with the volume fraction 3% and the pure water at different Marangoni numbers and $Ra_{\rm bf} = 10^4$. Comparing Figs. 3 and 4, we can clearly find that the strength of the primary flow circulations gets stronger, and the boundary layers at the hot and cold walls become denser when the Rayleigh number increases. The secondary flows are not prominent for

$$Ma_{\rm bf} \leqslant 100$$

when the gravity is strong enough. The strength of the primary flow circulations of the

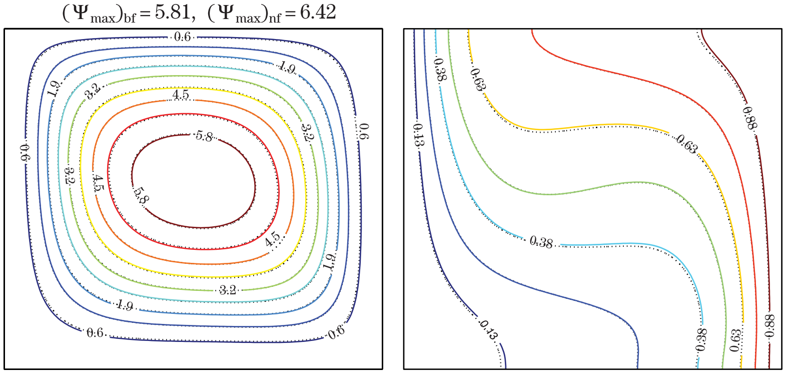
$(\Psi_{\max})_{\mathrm{bf}} = 5.81$, $(\Psi_{\max})_{\mathrm{nf}} = 6.42$

(a) Streamlines at *Ma* = 10 (b) Isotherms at *Ma* = 10

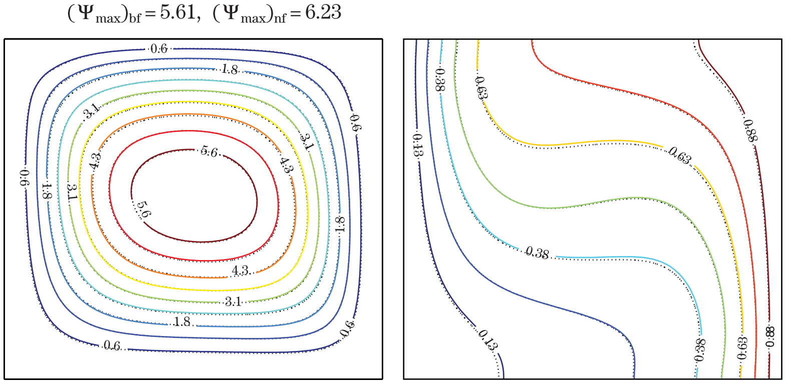
$(\Psi_{\max})_{\mathrm{bf}} = 5.61$, $(\Psi_{\max})_{\mathrm{nf}} = 6.23$

(c) Streamlines at *Ma* = 100 (d) Isotherms at *Ma* = 100

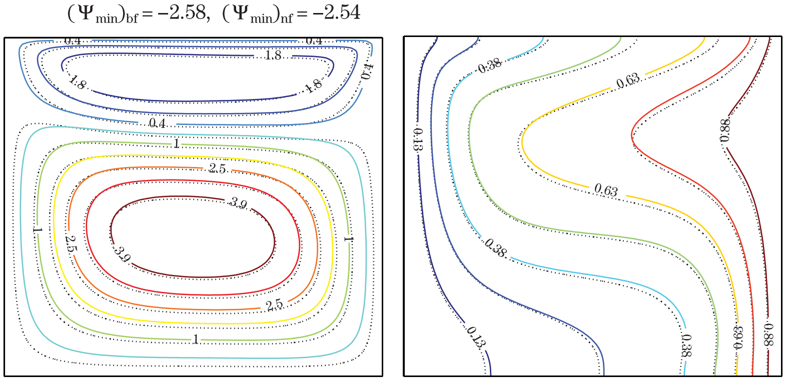
$(\Psi_{\min})_{\mathrm{bf}} = -2.58$, $(\Psi_{\min})_{\mathrm{nf}} = -2.54$

(e) Streamlines at *Ma* = 1 000 (f) Isotherms at *Ma* = 1 000

Fig. 4 Steady state streamlines and isotherms: water-Cu nanofluids with $\phi = 0.03$, solid lines; pure water for different Marangoni numbers at $Ra_{\mathrm{bf}} = 10^4$, dashed lines

nanofluids is stronger than that of the base fluid. The strong imbalance of the tangential stress on the interface suppresses these circulations, and forces them to the bottom cavity (see Fig. 4(c)). The cells of the primary base fluids locate closer to the bottom wall than the nanofluid cells. The strength of the negative flow circulations of the nanofluids is slightly weaker than that of the base fluid. The isotherms display a boomerang-shape. The signals of the convective thermocapillary at the top portion and the buoyancy force at the bottom portion have similar strength. The isotherms of the base fluids are more distorted at the top portion, while the isotherms of the base fluids are less distorted than the nanofluid isotherms at the bottom portion of the cavity. This unusual behavior does not happen when $Ma_{\rm bf} < 1\,000$ (see Figs. 4(a) and 4(b)) due to the relative small thermocapillary force.

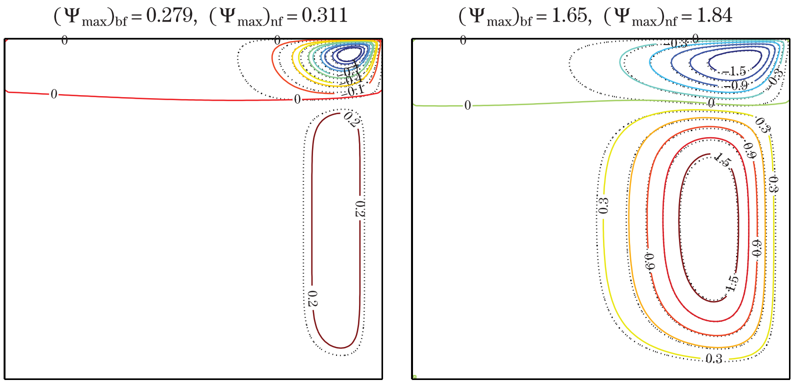

(a) $\tau = 0.003$ (b) $\tau = 0.010$

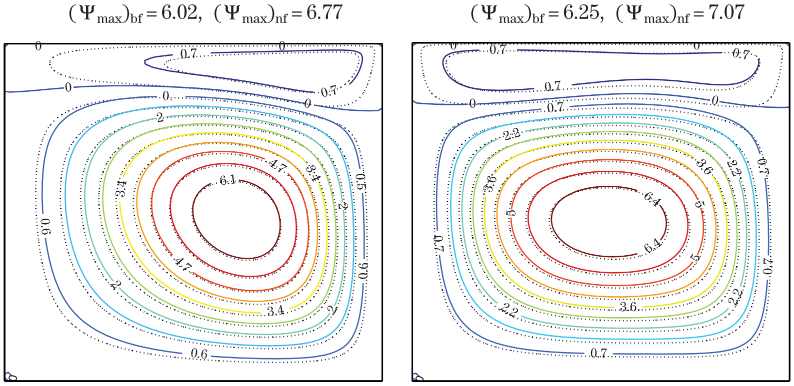

(c) $\tau = 0.030$ (d) $\tau = 0.050$

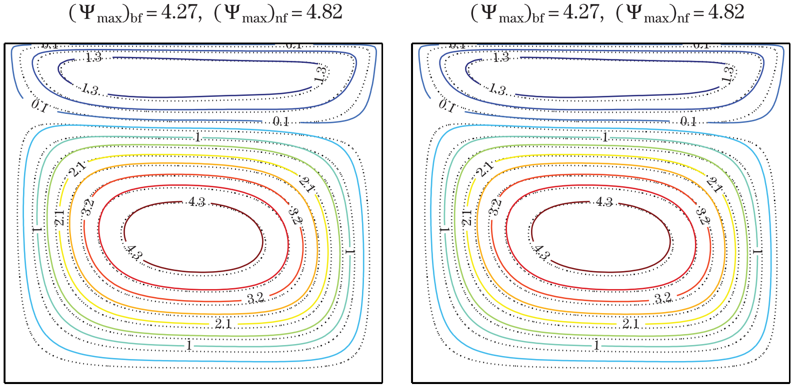

(e) $\tau = 0.400$ (f) $\tau = 0.700$

Fig. 5 Streamlines when $Ma_{\rm bf} = 750$ and $Ra_{\rm bf} = 10^4$ at $\tau = 0.003$, 0.010, 0.030, 0.050, 0.400, 0.700: nanofluids with $\phi = 0.03$, solid lines; pure-fluid for water-Cu, dashed lines

Figure 5 illustrates the time history of the streamlines for water and water-Cu nanofluids when

$$Ma_{\rm bf} = 750, \quad Ra_{\rm bf} = 10^4, \quad \tau = 0.003,\ 0.010,\ 0.030,\ 0.050,\ 0.400,\ 0.700.$$

The time history of the flow field is described as follows. Initially, at

$$\tau = 0.000,$$

the left and right walls are cold, and there is no fluid motion inside the cavity. When heating is started, i.e.,

$$\tau = 0.003,$$

the fluid temperature increases due to the heat from the hot-right wall. The fluid moves from the right region of the cavity to the left region due to the buoyancy force. This movement creates the primary cells in the lower portion. The cells are elongated vertically. At the same time, the circular cells are developed in the right-upper portion of the cavity. These secondary cells are caused by the surface tension effect. At

$$\tau = 0.010,$$

both the primary cells and the secondary cells get bigger and stronger, and occupy one half of the enclosure. As time goes on, the anti-clockwise and clockwise circulation cells occupy the whole enclosure, and the strength increases significantly. The core of the main cells moves to the center of the enclosure at

$$\tau = 0.050,$$

and the strength of the anti-clockwise flow circulations decreases. At the same time, the core of the secondary cells widens and fills almost the whole top region. This motion finally becomes permanent at

$$\tau = 0.400.$$

This means that increasing time further will not affect the flow pattern. We also observe that the strength of the primary flow circulations of the nanofluids is always stronger than that of the base fluid.

Figure 6 illustrates the time history of isotherms for water and water-Cu nanofluids when

$$\begin{cases} Ma_{\mathrm{bf}} = 750, \quad Ra_{\mathrm{bf}} = 10^4, \\ \tau = 0.003, 0.010, 0.030, 0.050, 0.400, 0.700. \end{cases}$$

The time history of the temperature field is described as follows. From Figs. 6(a) and 6(b), we can see that, at the very beginning, i.e.,

$$\tau = 0.003, \quad \tau = 0.010,$$

the isotherms for the nanofluids and base fluids are almost parallel and vertical. This implies that the conduction or diffusion mode is superior compared with convection. From Fig. 6(c), we can see that, at

$$\tau = 0.030,$$

the natural and Marangoni convection becomes superior compared with the conduction. As time goes on, the temperature is well distributed from the hot wall to the cold wall. The steady state mode is then achieved later. From

$$\tau = 0.003$$

to

$$\tau = 0.700,$$

the isotherms of the nanofluids and the base fluids in all regions exhibit distinct patterns.

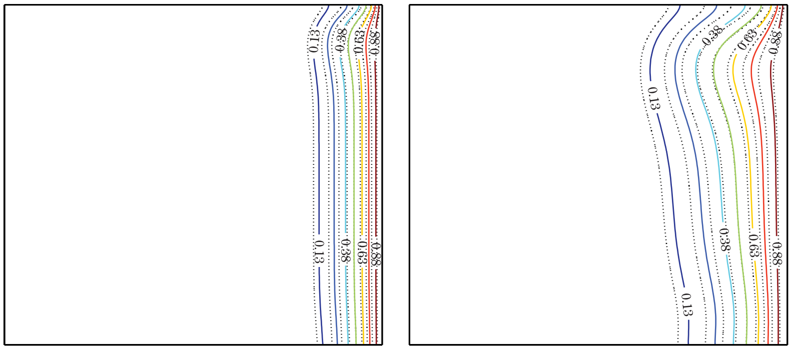

(a) $\tau = 0.003$ (b) $\tau = 0.010$

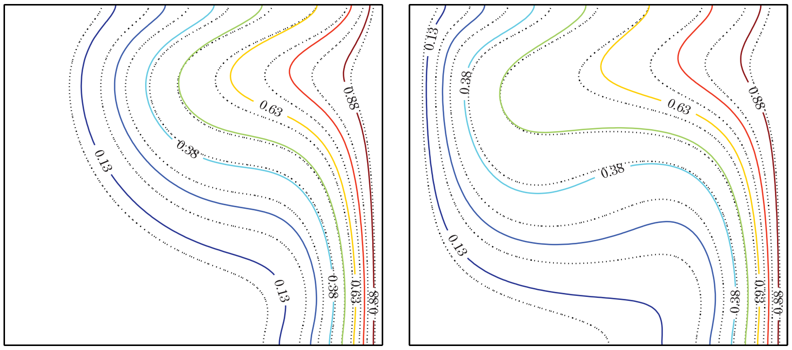

(c) $\tau = 0.030$ (d) $\tau = 0.050$

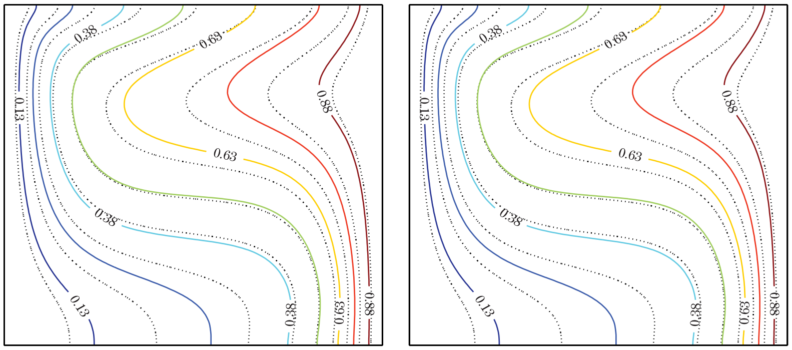

(e) $\tau = 0.400$ (f) $\tau = 0.700$

Fig. 6 Time history of isotherms with $Ma_{\rm bf} = 750$ and $Ra_{\rm bf} = 10^4$ at $\tau = 0.003$, 0.010, 0.030, 0.050, 0.400, 0.700: water-Cu nanofluids with $\phi = 0.03$, solid lines; pure water, dashed lines

Figure 7(a) shows the variations of the average Nusselt number along the cold wall and the hot wall for various $Ma_{\rm bf}$. At the early stages of the flow development, the average Nusselt number is identic for different $Ma_{\rm bf}$. When time goes on, $\overline{Nu}_{\rm c}$ increases, while $\overline{Nu}_{\rm h}$ decreases. The average Nusselt number is no longer identical. From the figure, we can also see that stronger thermocapillary force gives higher $\overline{Nu}$. The differences grow explicitly with time going on. After reaching a specific time, the value of $\overline{Nu}$ is kept constant when τ varies, or in other words, the steady condition is achieved. The numerical values of $\overline{Nu}$ at

$$Ra_{\rm bf} = 10^3$$

reach their respective steady conditions earlier than the numerical values of $\overline{Nu}$ at

$$Ra_{\mathrm{bf}} = 10^4$$

(see Figs. 3 and 4). The $\overline{Nu}$ profiles exhibit different tendencies when Ma_{bf} increases. Initially, $\overline{Nu}$ at the cold surface increases with the increase in the Marangoni number for fixed time. Moreover, the lowest Ma_{bf} gives the highest value for $\overline{Nu}$ at the hot surface under the steady condition.

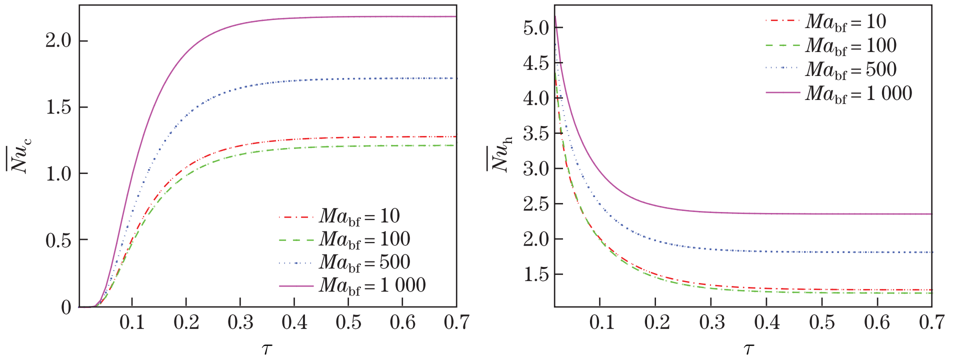

(a) $\overline{Nu}_{\mathrm{c}}$ at $Ra = 10^3$ (b) $\overline{Nu}_{\mathrm{h}}$ at $Ra = 10^3$

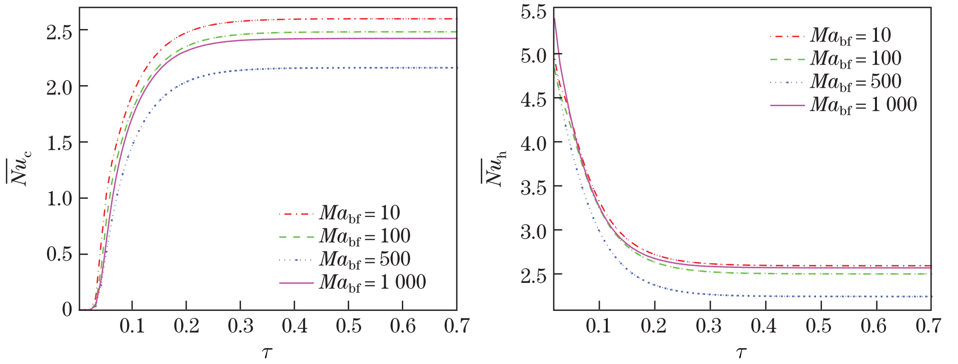

(c) $\overline{Nu}_{\mathrm{c}}$ at $Ra = 10^4$ (d) $\overline{Nu}_{\mathrm{h}}$ at $Ra = 10^4$

Fig. 7 Variations of $\overline{Nu}_{\mathrm{c}}$ and $\overline{Nu}_{\mathrm{h}}$ with time τ for different Ma with 5% Cu nanoparticles at $Ra_{\mathrm{bf}} = 10^3$ and $Ra_{\mathrm{bf}} = 10^4$

Figure 8 displays the average Nusselt number along the cold wall and the hot wall against the volume fraction for different nanoparticles at

$$Ra_{\mathrm{bf}} = 10^4.$$

The results demonstrated in this figure help to compare the heat transfer of Ag, Cu, Al_2O_3, or TiO_2 suspended in the water. The results show that the heat transfer rate for TiO_2 is the lowest (see Fig. 2 and Table 1). From Fig. 2, we can also see that increasing ϕ will increase the thermal conductivity ratio monotonically, and eventually lead to a monotonic increase in the heat transfer rate. When 1% ϕ of Ag, Cu, Al_2O_3, and TiO_2 increase, $\overline{Nu}_{\mathrm{c}}$ increases about 1.4%, 1.3%, 1.2%, and 1.2%, respectively. When 1% ϕ of Ag, Cu, Al_2O_3, and TiO_2 increase, $\overline{Nu}_{\mathrm{h}}$ increases about 1.5%, 1.4%, 1.3%, and 1.3%, respectively. These results signify that the hot wall is more sensitive to the adding nanoparticles.

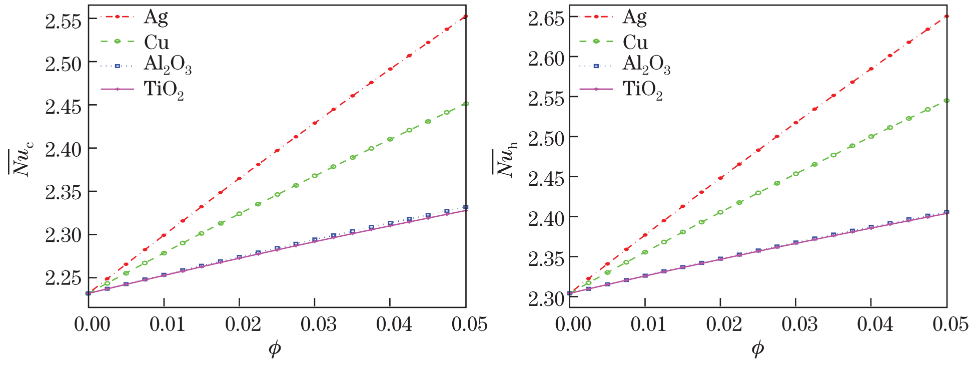

(a) $\overline{Nu}_c$ (b) $\overline{Nu}_h$

Fig. 8 Variations of $\overline{Nu}_c$ and $\overline{Nu}_h$ with ϕ for nanoparticles at $Ra_{bf} = 10^4$, $Ma_{bf} = 1\,000$, and steady state

Figure 9 shows the average Nusselt number along the cold and hot walls against the Marangoni number for different Cu concentrations at

$$Ra_{bf} = 10^4$$

in the steady state. As shown in the figure, Ma_{bf} varies from 0 to 1 000. In general, increasing the nanoparticle concentration increases $\overline{Nu}_c$ and $\overline{Nu}_h$. It is observed that the effect of adding the nanoparticles is insignificant when Ma_{bf} is about 250. Figure 9 also shows that the Nusselt number shows a minimum at the Marangoni number of roughly 500 for pure water ($\phi = 0.00$). The location of the minimum moves at a higher Cu concentration.

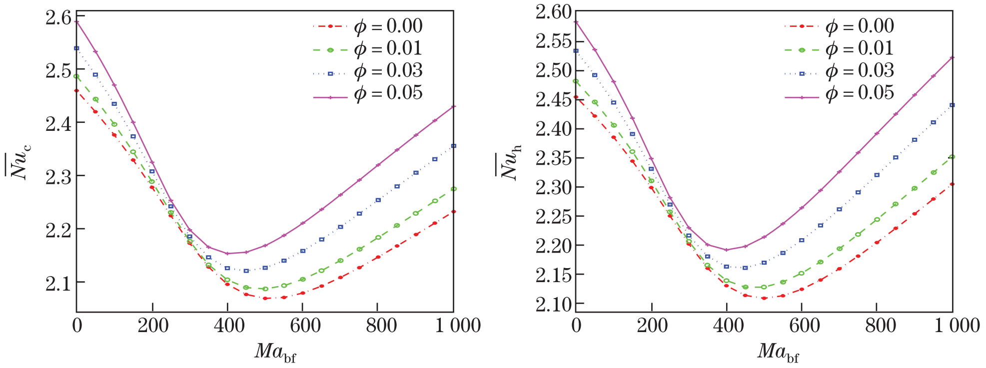

(a) $\overline{Nu}_c$ (b) $\overline{Nu}_h$

Fig. 9 Variations of $\overline{Nu}_c$ and $\overline{Nu}_h$ with Ma for different ϕ at $Ra_{bf} = 10^4$, water-Cu, and steady state

5 Conclusions

The effects of the nanoparticle types and the concentration on the buoyant Marangoni convection in a differentially heated square cavity are studied. The dimensionless forms of the governing equations are solved with the FD scheme consisting of the ADI method and the TDMA. The obtained results for the flow and temperature field and the average Nusselt number are presented in graphs. The main conclusions of the present analysis are as follows:

(i) For the convective thermocapillary and buoyancy force with similar strength, when the nanoparticle concentration increases, the flow rates in the primary cells increase, while the flow rates in the secondary cells decrease.

(ii) The average Nusselt number on the cold wall increases smoothly while the average Nusselt number on the hot wall decreases smoothly when time goes on. The steady state average Nusselt numbers on both the cold wall and the hot wall increase when the nanoparticle concentration increases. Moreover, the average Nusselt number on the hot wall is slightly higher than the average Nusselt number on the cold wall.

(iii) A critical Marangoni number exists, below which the average Nusselt number decreases when the Marangoni number increases, and above which the average Nusselt number increases when the Marangoni number increases. The nanoparticles play a crucial role in the critical Marangoni number.

References

[1] Chandrasekhar, S. *Hydrodynamics and Hydromagnetic Stability*, Oxford University, Clarendon Press, Oxford (1961)

[2] Pearson, J. R. On convection cells induced by surface tension. *Journal of Fluid Mechanics*, **4**, 489–500 (1958)

[3] Strani, M., Piva, R., and Graziani, G. Thermocapillary convection in a rectangular cavity: asymptotic theory and numerical simulation. *Journal of Fluid Mechanics*, **130**, 347–376 (1983)

[4] Srinivasan, J. and Basu, B. A numerical study of thermocapillary flow in a rectangular cavity during laser melting. *International Journal of Heat and Mass Transfer*, **29**, 563–572 (1986)

[5] Bergman, T. L. and Ramadhyani, S. Combined buoyancy- and thermocapillary-driven convection in open square cavities. *Numerical Heat Transfer*, **9**, 441–451 (1986)

[6] Carpenter, B. M. and Homsy, G. M. Combined buoyant-thermocapillary flow in a cavity. *Journal of Fluid Mechanics*, **207**, 121–132 (1989)

[7] Hadid, H. B. and Roux, B. Buoyancy and thermocapillary-driven flows in differentially heated cavities for low-Prandtl number fluids. *Journal of Fluid Mechanics*, **235**, 1–36 (1992)

[8] Rudraiah, N., Venkatachalappa, M., and Subbaraya, C. K. Combined surface tension and buoyancy-driven convection in a rectangular open cavity in the presence of a magnetic field. *International Journal of Non-Linear Mechanics*, **30**, 759–770 (1995)

[9] Hossain, M. A., Hafiz, M. Z., and Rees, D. A. S. Buoyancy and thermocapillary driven convection flow of an electrically conducting fluid in an enclosure with heat generation. *International Journal of Thermal Sciences*, **44**, 676–684 (2005)

[10] Saleem, M., Hossain, M. A., Mahmud, S., and Pop, I. Entropy generation in Marangoni convection flow of heated fluid in an open ended cavity. *International Journal of Heat and Mass Transfer*, **54**, 4473–4484 (2011)

[11] Choi, S. U. S. Enhancing thermal conductivity of fluids with nanoparticles. *Developments and Applications of Non-Newtonian Flows*, ASME, New York, 99–105 (1995)

[12] Khanafer, K., Vafai, K., and Lightstone, M. Buoyancy-driven heat transfer enhancement in a two-dimensional enclosure utilizing nanofluids. *International Journal of Heat and Mass Transfer*, **46**, 3639–3653 (2003)

[13] Jou, R. Y. and Tzeng, S. C. Numerical research of nature convective heat transfer enhancement filled with nanofluids in rectangular enclosures. *International Communications in Heat and Mass Transfer*, **33**, 727–736 (2006)

[14] Das, M. K. and Ohal, P. S. Natural convection heat transfer augmentation in a partially heated and partially cooled square cavity utilizing nanofluids. *International Journal of Numerical Methods for Heat and Fluid Flow*, **19**, 411–431 (2009)

[15] Ghasemi, B. and Aminossadati, S. M. Natural convection heat transfer in an inclined enclosure filled with a water-CuO nanofluid. *Numerical Heat Transfer*, *Part A*: *Applications*, **55**, 807–823 (2009)

[16] Oztop, H. F. and Abu-Nada, E. Numerical study of natural convection in partially heated rectangular enclosures filled with nanofluids. *International Journal of Heat and Fluid Flow*, **29**, 1326–1336 (2008)

[17] Öğüt, E. B. Natural convection of water-based nanofluids in an inclined enclosure with a heat source. *International Journal of Thermal Sciences*, **48**, 2063–2073 (2009)

[18] Hwang, K. S., Lee, J. H., and Jang, S. P. Buoyancy-driven heat transfer of water-based Al_2O_3 nanofluids in a rectangular cavity. *International Journal of Heat and Mass Transfer*, **50**, 4003–4010 (2007)

[19] Santra, A. K., Sen, S., and Chakraborty, N. Study of heat transfer characteristics of copper-water nanofluid in a differentially heated square cavity with different viscosity models. *Journal of Enhanced Heat Transfer*, **15**, 273–287 (2008)

[20] Rashmi, W., Ismail, A. F., Khalid, M., and Faridah, Y. CFD studies on natural convection heat transfer of Al_2O_3-water nanofluids. *Heat and Mass Transfer*, **47**, 1301–1310 (2011)

[21] Ho, C. J., Chen, M. W., and Li, Z. W. Numerical simulation of natural convection of nanofluid in a square enclosure: effects due to uncertainties of viscosity and thermal conductivity. *International Journal of Heat and Mass Transfer*, **51**, 4506–4516 (2008)

[22] Qi, C., He, Y., Hu, Y., Yang, J., Li, F., and Ding, Y. Natural convection of Cu-Gallium nanofluid in enclosures. *Journal of Heat Transfer*, **133**, 122504 (2011)

[23] He, Y., Qi, C., Hu, Y., Qin, B., Li, F., and Ding, Y. Lattice Boltzmann simulation of alumina-water nanofluid in a square cavity. *Nanoscale Research Letters*, **6**, 184 (2011)

[24] Fattahi, E., Farhadi, M., Sedighi, K., and Nemati, H. Lattice Boltzmann simulation of natural convection heat transfer in nanofluids. *International Journal of Thermal Sciences*, **52**, 137–144 (2012)

[25] Brinkman, H. C. The viscosity of concentrated suspensions and solutions. *Journal of Chemical Physics*, **20**, 571–581 (1952)